J. Fluid Mech. (1977), *vol.* 83, *part* 4, *pp.* 641–671
Printed in Great Britain

A time-domain analysis of the large-scale flow structure in a circular jet. Part 1. Moderate Reynolds number

By H. H. BRUUN
Engineering Laboratory, University of Cambridge

(Received 28 May 1976 and in revised form 14 March 1977)

This paper presents a new experimental time-domain technique for the evaluation of the large-scale structure in a turbulent flow. The technique is demonstrated by hot-wire anemometry for a circular jet flow at a moderate Reynolds number of 10^4, and the large-scale structure identified is compared successfully with smoke flow-visualization observations. The temporal and spatial relationships of the separate large-scale flow events have been derived, and this information enabled the evaluation of the nonlinear spatial development of the large-scale flow structure.

1. Introduction

The flow processes which occur in turbulent flows have been investigated for more than fifty years. Early flow-visualization experiments on turbulent flows revealed what appeared to be nearly irregular flow phenomena, and the fluctuating signals measured with fast-responding instruments such as hot-wire probes and miniature pressure transducers were therefore initially evaluated by conventional statistical methods and the results interpreted in terms of random processes.

The improved flow-visualization experiments on turbulent boundary layers by Kline in the 1960s and many subsequent investigations have, however, revealed that semi-regular flow structures can be identified in turbulent flows. Furthermore, with the advent of fast digital computers, conditional sampling techniques have been developed which enable separate flow phenomena to be isolated and studied. All these developments point towards the existence of a more orderly structure in turbulent flows than was previously supposed.

The purpose of this investigation was to identify the large-scale flow structure in a circular jet flow. A large number of experimental investigations of axisymmetric jet flows, using both conventional and conditionally sampled statistics, have been reported by research workers at the Institute of Sound and Vibration Research, Southampton University. The results presented in this paper were derived from an initial attempt to improve the conditional sampling technique described by Lau & Fisher (1975). One of the disadvantages of their technique, as recognized by the authors themselves, was the very small amplitude of the recovered signal. The initial step in this investigation was a study of criteria which might result in a larger amplitude of the recovered signal. It soon became clear, however, that very little improvement could be obtained. It therefore became necessary to review the whole

principle of Lau & Fisher's conditional sampling technique, and the very simple vortex-ring model which they used for the interpretation of their data.

As a result of this review a new time-domain technique has been developed which can identify the large-scale flow structure in a fluid flow from hot-wire probes placed in the flow field. To demonstrate the validity of this new method, in part 1 of this study it is applied to a transitional circular air jet with a moderate Reynolds number Re of 10^4, in which a semi-regular axisymmetric large-scale flow structure has previously been observed in flow-visualization experiments (Wehrmann & Wille 1958; Wille 1963; Freymuth 1966; Becker & Massaro 1968; Crow & Champagne 1971).

Observation of the flow structure by flow visualization and high-speed photography has the advantage that it provides information on both the temporal and the spatial development of the regular flow structure, i.e. a Lagrangian description of the flow processes. Measurements with fast-responding tranducers which are placed at fixed points in the flow field, however, only provide information in an Eulerian frame of reference. Transformation of the time-history signals from the fixed probes into the flow structure of the disturbances which move past the probes represents one of the greatest unsolved problems in experimental fluid mechanics. The existence of regular flow structures has therefore until now largely been inferred from very simplified assumptions such as frozen-pattern convection. In this paper, however, by applying the new time-domain technique to a transitional circular air jet with a nozzle Reynolds number of 10^4, it is demonstrated that it *is* possible to evaluate the *average* large-scale flow structure which moves past the fixed hot-wire probes from the measured velocity signals.

By performing smoke flow-visualization experiments at the same Reynolds number it is demonstrated in this paper that the average large-scale flow structure observed by flow visualization is identical to the large-scale flow structure derived by the new time-domain technique.

Flow-visualization experiments, however, have failed to reveal the existence of an orderly large-scale flow structure in turbulent air jets ($Re > 10^5$). Having proved the validity of the time-domain technique (part 1), the method was then used to investigate the large-scale flow structure which may exist in a turbulent air jet ($Re = 2 \times 10^5$), and the results obtained are presented in part 2 of this study.

Until recently flow structures were either derived from flow-visualization experiments or inferred from conventional statistical measurements. Therefore before presenting the new time-domain technique, and the derivation of the large-scale flow structure existing at a nozzle Reynolds number of 10^4, a short discussion of corresponding conventional statistical measurements (§ 3) and the large-scale flow structure observed by flow visualization (§ 4) will be presented.

2. Experimental set-up

In the present investigation a 5·08 cm diameter nozzle with an area contraction ratio of 9:1 was used. The nozzle was supplied with air from carbon-ringed oil-free compressors through a system of driers, reservoirs and filters before entering the settling chamber of the jet rig. The same jet rig was used in the investigations by Davies, Fisher & Barratt (1963), Ko & Davies (1971, 1975), Lau, Fisher & Fuchs (1972) and Lau & Fisher (1975).

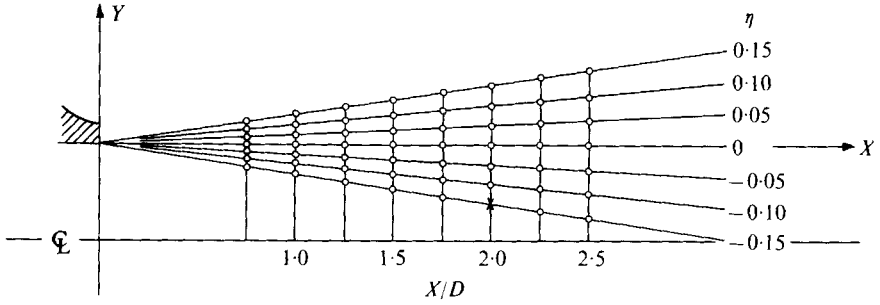

FIGURE 1. Air-jet co-ordinate system and hot-wire positions.
×, fixed wire; ○, eduction wire. $Re = 10^4$.

Standard 2 mm ISVR hot-wire probes (Davies 1974; Bruun 1975) were used for measuring the instantaneous velocities. The results presented in part 1 of this study were obtained with normal hot-wire probes, while both normal and X-wire probes were used in the investigation of the turbulent air jet (part 2).

The hot-wire probes were used in conjunction with the constant-temperature anemometer and linearizer unit developed at the Institute of Sound and Vibration Research (Davies 1974). The linear output from the anemometer set was selected to simplify the data processing. The calibration and adjustment of the linearizer unit in the ISVR anemometer set are minimal, and the linearization obtained has been shown to be of adequate accuracy (Bruun 1971). The frequency response of the anemometer is flat from d.c. to 20 kHz, which was sufficient for the present investigation.

The data processing was carried out on a Myriad digital computer. The linear anemometer output from one or two hot-wire probes was connected on line to the computer via an A/D converter having two parallel inputs and a maximum sampling rate of 20000 samples/s. The maximum input voltage to the A/D convertor was ± 10 V, enabling the acquisition of the total instantaneous velocity signals, which were stored directly on a 2 M word magnetic disc. In the subsequent analysis the original acquired data were retained, so that both conventional statistics and conditionally sampled evaluations could be carried out on the same data.

3. Initial conventional statistical measurements

Initial measurements were carried out over the first five diameters downstream of the nozzle exit. Previous measurements at high Reynolds numbers (Davies *et al.* 1963; Ko & Davies 1971) have demonstrated that the mean velocity and turbulence intensity profiles at different axial positions are nearly identical when the radial probe position is expressed in terms of the parameter

$$\eta = Y/X, \tag{1}$$

where X and Y are the co-ordinates defined in figure 1. The probe positions in this investigation were consequently selected on constant-η lines as shown in figure 1. It will, however, be demonstrated in § 7 that derivation of the large-scale flow

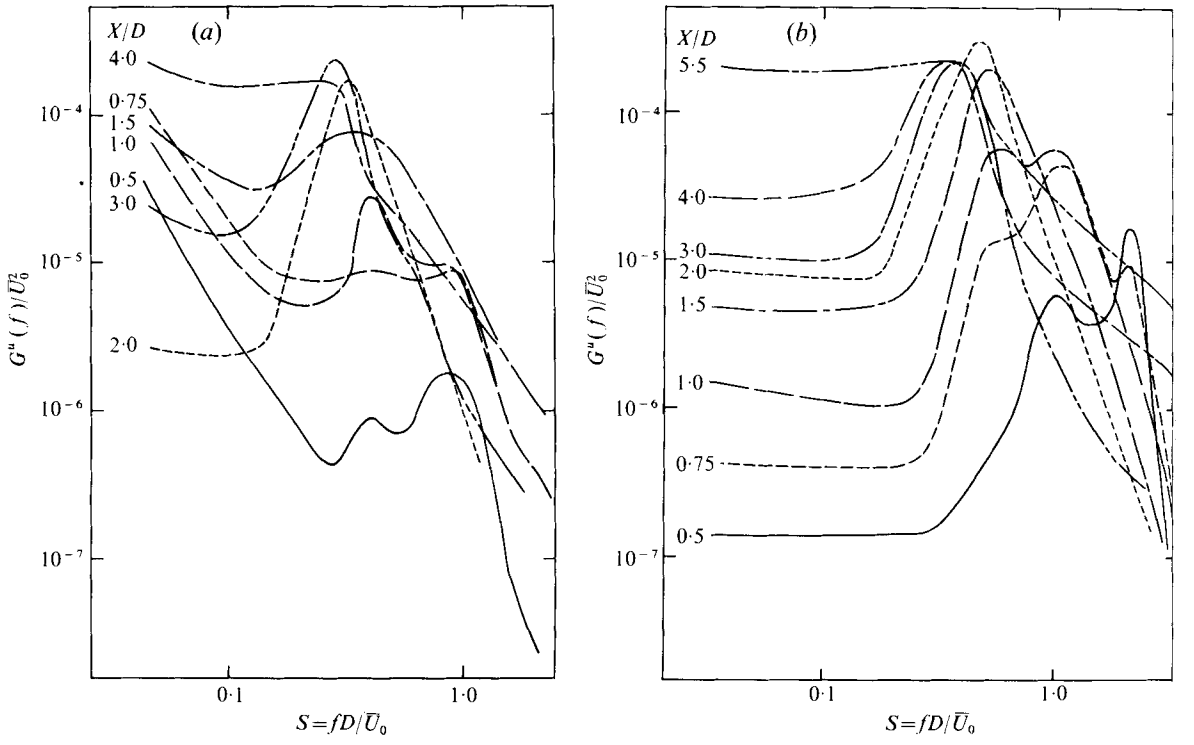

FIGURE 2. Axial variation in the u-component velocity spectrum in the potential core ($\eta = -0{\cdot}15$). (*a*) $Re = 7{\cdot}1 \times 10^3$. (*b*) $Re = 2{\cdot}1 \times 10^4$.

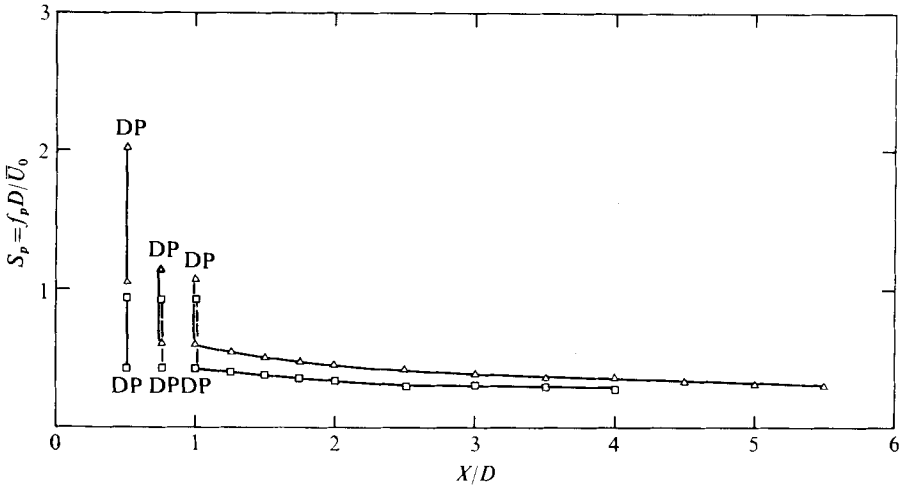

FIGURE 3. Axial variation in the potential-core Strouhal number ($\eta = -0{\cdot}15$) for two different Reynolds numbers. DP, double peaks in the u-component velocity spectrum; □, $Re = 7{\cdot}1 \times 10^3$; △, $Re = 2{\cdot}1 \times 10^4$.

structure is not restricted to selection of points on constant-η lines. All the measurements presented in part 1 of this study were confined to one X, Y plane, as the flow-visualization experiments demonstrated that the large-scale flow structure was axisymmetric at moderate Reynolds numbers (§ 4).

The results discussed in this section were obtained from a single normal hot-wire probe placed at different points in the jet flow. The output signal from a normal hot-wire probe will, for all practical purposes, give information on the velocity component in the axial direction. Only in the outer part of the mixing layer, where the local turbulence intensity is high, may corrections be necessary (Bruun 1976).

The initial statistical measurements were selected to provide information concerning the axial development and Reynolds number variation of the large-scale flow structure existing in the present experimental investigation. Spectral analysis of the u velocity fluctuations in the potential core has demonstrated the existence of a pronounced peak in the spectrum (Bradshaw, Ferriss & Johnson 1964; Ko & Davies 1971) and the corresponding peak frequency can be related to the flow structure in the mixing region of the jet. The axial variation and Reynolds number dependence of the large-scale flow structure (at moderate Reynolds numbers) were consequently investigated by selecting two Reynolds numbers ($7{\cdot}1 \times 10^3$ and $2{\cdot}1 \times 10^4$) and carrying out spectral analyses for both Reynolds numbers at different axial positions along $\eta = -0{\cdot}15$. (For values of $X/D \geqslant 3$ the probe position was on the centre-line.) The measured spectra for the two Reynolds numbers are plotted in figures 2(a) and (b) as a function of the Strouhal number $S = fD/\bar{U}_0$, demonstrating both axial and Reynolds number variation.

At a Reynolds number of $7{\cdot}1 \times 10^3$ a single vortex-pairing process can be inferred from the axial variation in the spectra. For axial positions X/D between 0·5 and 1·0 a double peak exists in the velocity spectrum. At $X/D = 0{\cdot}5$ the peak with the higher frequency f_1 has the larger amplitude. As the flow moves downstream the amplitude of this peak decreases while the amplitude of the lower frequency peak f_2 increases ($X/D = 1{\cdot}0$), until at $X/D = 1{\cdot}5$ only the low frequency peak f_2 remains. The Strouhal numbers $S_p = f_pD/\bar{U}_0$ corresponding to the single or double peaks in the velocity spectra have been evaluated and the results are shown in figure 3. The ratio f_1/f_2 of the high and low peak frequencies is approximately 2, which corresponds to a single vortex-pairing process occurring close to the nozzle. The pairing process is seen to be completed at $X/D = 1{\cdot}5$. As the flow progresses further downstream ($1{\cdot}5 \leqslant X/D < 4$) a nearly constant value of the Strouhal number of 0·3 is observed, which is related to the axial convection of the regular large-scale vortex resulting from the single vortex-pairing process. The amplitude of the peak decreases with increasing axial position and at $X/D = 4{\cdot}0$ a peak can no longer be identified in the velocity spectrum.

When the Reynolds number is increased to $2{\cdot}1 \times 10^4$ a new vortex-pairing process occurs, as was also observed by Crow & Champagne (1971). Close to the nozzle ($X/D = 0{\cdot}5$) a double peak exists in the spectrum, the larger peak amplitude occurring at the higher frequency f_1. As we move downstream to $X/D = 0{\cdot}75$ the high frequency peak f_1 has decreased in amplitude and a new even lower frequency peak f_3 can just be observed in the spectrum. At $X/D = 1{\cdot}0$ the highest peak f_1 has completely disappeared, while the lowest peak f_3 has grown in amplitude to be of the same

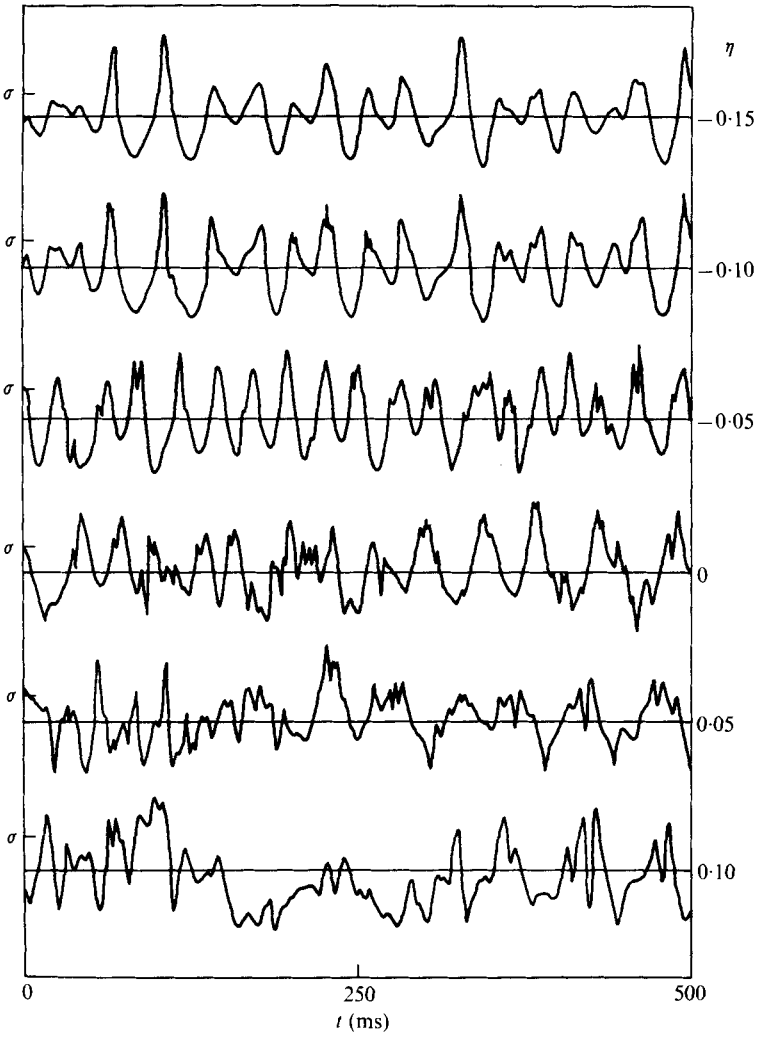

FIGURE 4. Time-history plots of the u velocity component at various radial positions at $X/D = 2{\cdot}0$. $Re = 10^4$.

magnitude as the peak f_2. Further downstream ($X/D = 1{\cdot}5$) only the lowest peak f_3 remains in the velocity spectrum.

The Strouhal number corresponding to the single and double peaks in the frequency spectra in figure 2(*b*) are also shown in figure 3. The ratios f_1/f_2 and f_2/f_3 of the double-peak frequencies are approximately 2, and these results can therefore be interpreted in terms of two sets of vortex-pairing processes, whereby four initial disturbances coalesce into one large vortex. This pairing process is completed at $X/D = 1{\cdot}5$, and a nearly constant Strouhal number S_p of 0·4 exists in the region $1{\cdot}5 \leqslant X/D \leqslant 5{\cdot}5$, corresponding to the downstream convection of the large vortices. The axial development of the regular vortex structure beyond $X/D > 1{\cdot}5$ is therefore different at the two Reynolds numbers $7{\cdot}1 \times 10^3$ and $2{\cdot}1 \times 10^4$.

These results are in agreement with the results of the flow-visualization experi-

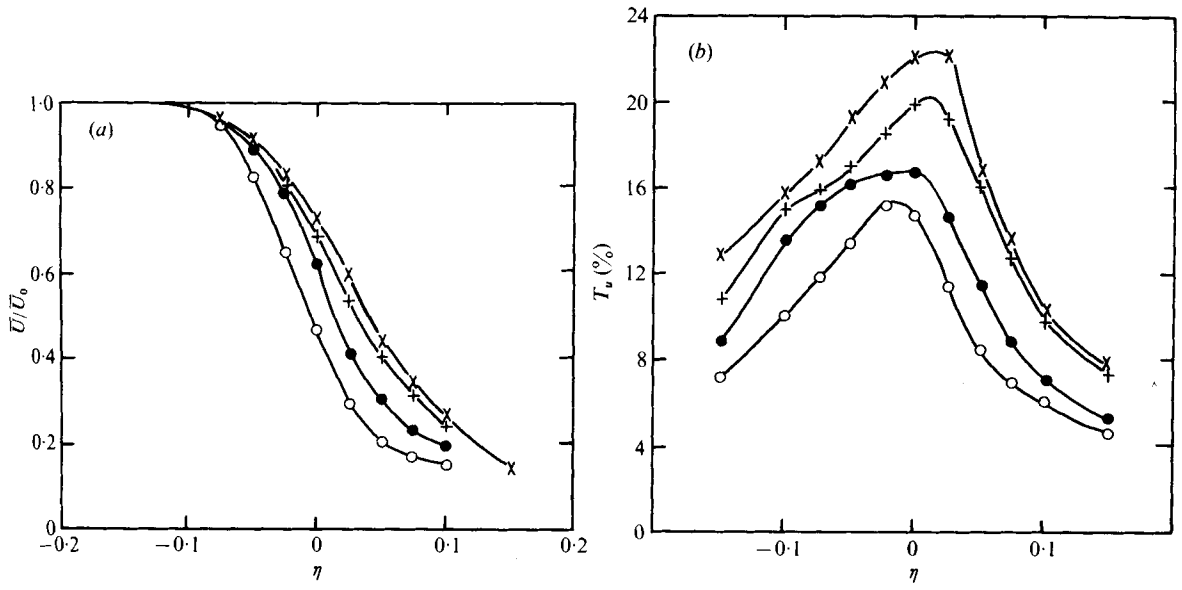

FIGURE 5. Development of (*a*) mean velocity profile and (*b*) turbulence intensity in the initial region. $Re = 10^4$. ○, $X/D = 0{\cdot}75$; ●, $X/D = 1{\cdot}0$; +, $X/D = 1{\cdot}25$; ×, $X/D = 2{\cdot}0$.

ments by Wille (1963), Becker & Massaro (1968) and Crow & Champagne (1971), which have demonstrated that a single vortex-pairing process occurs in the Reynolds number range $3 \times 10^3 < Re \leqslant 10^4$. It was consequently decided to investigate this vortex-pairing process to demonstrate the new time-domain technique, and a moderate Reynolds number Re of 10^4 was selected for this purpose.

At that Reynolds number a normal hot-wire probe was traversed radially at $X/D = 2{\cdot}0$, and the time histories of the fluctuating part of the u velocity component at different radial positions were recorded; typical results are shown in figure 4. To emphasize the shape of the velocity signals free scaling was used, and the local r.m.s. value of $\sigma = (\overline{u^2})^{\frac{1}{2}}$ is marked on each plot. The corresponding values of the turbulence intensity $T_u = \sigma/\bar{U}_0$ are plotted in figure 5 (*b*).

The velocity signals are seen to have a large amount of regularity in the whole of the interior of the mixing layer ($-0{\cdot}10 \leqslant \eta < 0$), while in the outer part of the mixing layer ($\eta > 0$) the plots show what *appear* to be irregular velocity time histories, and no conclusions regarding the existence of a regular large-scale structure can be deduced by visual inspection of these time records.

The vortex-pairing process takes place within the first two diameters downstream of the nozzle exit. The corresponding mean velocity and turbulence intensity distributions at different axial positions, plotted in figures 5 (*a*) and (*b*), consequently demonstrate a considerable axial development in the initial region of the jet.

Conventional statistical measurements have thus produced clear evidence for the existence of a regular large-scale flow structure in a transitional air jet at a moderate Reynolds number of 10^4. The spatial distribution and the temporal development of the flow structure, however, cannot be deduced from such measurements.

The existing large-scale flow structure is first illustrated by smoke flow-visualization experiments (§ 4). The principles of the new time-domain technique are described

in § 5, and the large-scale flow structure existing at the Reynolds number of 10^4 is then derived by the time-domain technique in §§ 6 and 7. A comparison of the flow-visualization and time-domain results and a discussion of the separate large-scale flow events are presented in § 8.

4. Flow-visualization experiment

Using smoke injection upstream of the nozzle exit, still pictures were taken of the large-scale flow structure existing at a moderate Reynolds number Re of 10^4 to confirm the large-scale flow structure obtained by the time-domain technique. The pictures were taken near the completion of the time-domain investigation but, to facilitate the explanation and understanding of the time-domain results, the flow structure observed by the flow-visualization technique will be presented first.

Previous flow-visualization experiments and the results obtained in the present investigation have demonstrated that the large-scale flow structure existing in the first three diameters downstream of the nozzle exit is axisymmetric at moderate Reynolds numbers. The time-domain measurements were consequently carried out in one axial/radial plane through the centre of the jet, and to obtain the corresponding flow structure in the smoke-filled jet only a thin cross-section of the jet was illuminated by a slit lighting technique. An electronic flash bulb placed on top of the jet was connected to a 250 mm long light-guide, which was positioned just outside the jet mixing layer along the axial direction. This enabled a 10 mm wide radial/axial cross-section to be illuminated (see figures 6(*a*)–(*c*), plate 1). Pictures containing the axial and radial positions of the large-scale flow events were obtained with a camera placed at 90° to the illuminated cross-section.

The large-scale flow structure obtained by the time-domain technique was derived for selected time/space positions of a given trigger event B (a large positive peak) on the line $\eta = -0{\cdot}15$. The signal from the hot-wire probe was used to trigger the flash bulb, the trigger criterion being the occurrence of a large positive peak above a preset trigger level, i.e. flow event B. Single pictures were obtained with a flash bulb controlled by a trigger unit with a manual reset. Typical pictures corresponding to a trigger event B occurring at the probe positions $X/D = 1{\cdot}5$, $2{\cdot}0$ and $2{\cdot}5$ are shown in figures 6(*a*)–(*c*).

The flow-visualization pictures clearly demonstrate that a nearly regular vortex structure can be identified close to the hot-wire probe at all three probe positions each time the specified trigger event B occurs. Furthermore, regular vortex structures are seen to follow the trigger event B, but the flow structure downstream of the trigger event B is seen to be less regular. The flow-visualization pictures also confirm that the large-scale flow structure is axisymmetric at moderate Reynolds numbers. The conventional statistical measurements (§ 3) indicated the existence of a single vortex-pairing process close to the nozzle exit ($X/D \leqslant 2$), and the final stage of such a vortex-pairing process is clearly visible in figure 6(*a*), at $X/D \simeq 1{\cdot}5$.

Several pictures were taken for each probe position. Similar flow events could be identified on all the pictures, but considerable spatial variations were observed between different photographs. To enable comparison with the time-domain results it was therefore necessary to evaluate the *average* flow-visualization flow structure

from these photographs. The resulting average flow-visualization flow structure and the comparison with the time-domain results are discussed in § 8.

The large-scale flow structure existing in a circular air jet at a moderate Reynolds number of 10^4 has now been identified. To demonstrate the validity of the new time-domain technique, we now proceed *independently* to derive the same large-scale flow structure from hot-wire probes placed at fixed points in the flow field.

As the large-scale flow structure has been shown to be axisymmetric, we need consider only the u (axial) and v (radial) components of the velocity vector. Simultaneous measurements of the u and v components greatly facilitate the interpretation of the time-domain results, as discussed in § 8 below and in part 2 of this study. In part 1, however, only the u component was measured, but it is demonstrated that it is possible from measurements of only this component to derive the average large-scale flow structure in the jet.

5. The time-domain technique

A normal hot-wire probe placed at a fixed point in a jet flow records the u velocity component of the flow as it moves past the probe. A time record from a single hot-wire probe is therefore not sufficient to determine the spatial distribution and the temporal development of the large-scale flow structure. The basic information concerning the large-scale flow structure is, however, contained in the signal from a fixed hot-wire probe and the large-scale flow structure can be derived if more than one probe is used.

Consider two hot-wire probes A and B placed in the flow field. If a large-scale flow event is detected by probe A then it can also be recognized in the signal from probe B, *provided* that the flow event remains coherent in the time interval and over the space specified by the two probe positions. Therefore *each* time a *particular* large-scale flow event occurs at the fixed probe position A, a *similar* nearly regular large-scale flow event can be identified in the signal from a probe B placed close to probe A. This must be true for *any* spatial position of probe B relative to the fixed probe A. Consequently, if the velocity fluctuations from closely spaced points in the flow field were measured simultaneously, then it would in principle be possible to evaluate all the flow processes occurring in the jet flow. In practice, however, two limitations exist. First, only a very limited number of probes can be used, and to cover the flow field investigated these probes must be placed consecutively in different parts of the flow field. Owing to limitations on experimental time and computational costs the number of measuring points is restricted, and a not insignificant separation s therefore exists between the different probe positions. As a result 'small-scale' flow events which are not sustained in time and space over at least two or three axial probe positions cannot be identified from the corresponding measurements. The separation of the flow structure into 'large-scale' and 'small-scale' flow events is therefore ambiguous and can be a function of the mesh size of the selected measuring grid. In principle, investigations using a small probe separation s should be able to identify smaller-scale flow events than an experiment with a large probe separation s. However, as the number of measuring points is limited, one is usually forced to choose between a grid of measuring points with a fine mesh size in a small part of the flow field or a

coarse grid covering a large part of the flow field. For clarity a coarse grid with an axial separation of $\Delta X/D = 0{\cdot}25$ between probe positions (figure 1) was selected in this investigation.

Second, the number of probes is usually much smaller than the number of measuring points, and simultaneous measurements at all probe positions are therefore not possible. However, each time a regular large-scale flow event occurs at a fixed hot-wire probe A, a nearly regular large-scale flow event can also be identified in the signal from other measuring points in the grid. The large-scale flow events can therefore be obtained by using a fixed hot-wire probe in conjunction with a second hot-wire probe which is placed consecutively at all the points in the selected grid. The new technique for the evaluation of the large-scale flow events must therefore involve conditionally sampled data in the time domain, and the corresponding data processing was performed on a Myriad digital computer.

The basic data for this new technique are the two simultaneous time records of the u velocity component from the fixed and the moving hot-wire probes. A complete set of such simultaneous time records corresponding to all the moving hot-wire probe positions (figure 1) was acquired by the computer via the A/D converter and stored on a magnetic disc.

The new time-domain technique for the evaluation of the large-scale flow events consists of three separate parts:

(i) A trigger criterion for the identification and selection of a particular type of flow event (trigger event) in the signal from the fixed hot-wire probe.

(ii) An eduction technique to retrieve that part of the moving-wire signal which is related to the trigger event (educed signal).

(iii) An interpretation method for relating the educed signals at all the measurement points to the corresponding large-scale flow structure.

It is in the last respect that the present paper makes its major contributions.

5.1. *Trigger criterion*

The selection of a trigger criterion involves the spatial position of the fixed hot-wire probe and the identification of a signal pattern which is related to a *particular* large-scale flow event.

The fixed hot-wire probe can be placed either in the mixing region or in the potential core of the jet flow. A hot-wire probe placed in the mixing region records the flow events as they are convected past the wire, while a hot-wire probe placed in the potential core measures the velocity fluctuations induced by the flow processes occurring in the mixing region. Shortlived small-scale flow processes in the mixing region are usually not reflected in the potential-core velocity fluctuations, which are mainly related to the large-scale flow events. To give a clear demonstration of the new technique, the fixed hot-wire probe was therefore placed in the potential core of the jet flow ($X/D = 2{\cdot}0$, $\eta = -0{\cdot}15$) in part 1 of this study. Different large-scale flow events may, however, be deduced if the fixed hot-wire probe is placed in the mixing region. This aspect was also investigated and the corresponding results are presented in part 2 of this study.

At the beginning of this investigation no information was available on how to relate the signal pattern to particular large-scale flow events. However, each time a

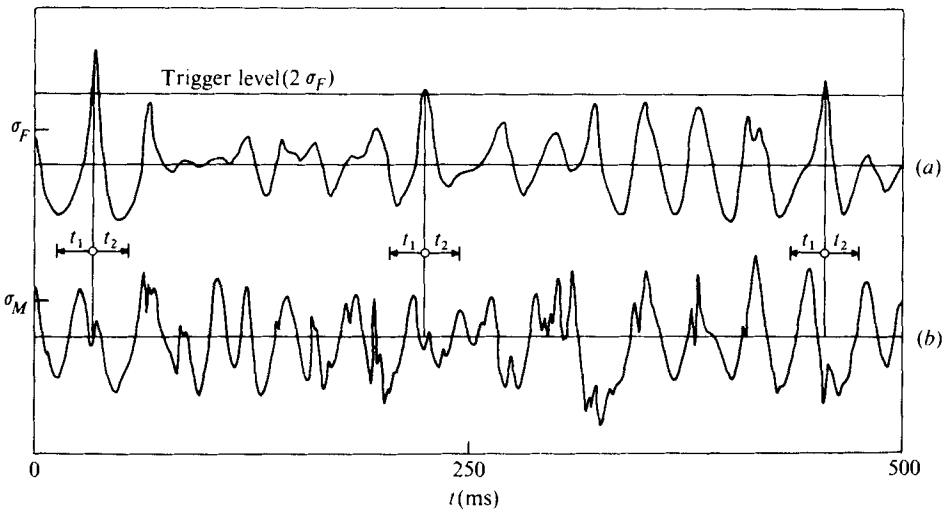

FIGURE 7. Eduction principle. $Re = 10^4$. (*a*) Fixed (trigger) wire: $X/D = 2{\cdot}0$; $\eta = -0{\cdot}15$. (*b*) Moving (eduction) wire: $X/D = 2{\cdot}0$; $\eta = -0{\cdot}025$.

large positive peak occurs in the u velocity signal the hot wire is in a part of the flow which moves faster than the average velocity. If it can be shown that the corresponding flow event is sustained in time and space, then a particular large-scale flow event has been identified. Measurements were consequently carried out, and the results (§ 5.4.1) conclusively established the relationship between large positive peaks and a particular fast-moving large-scale flow event. Similarly a large negative peak was shown to be related to a particular slow-moving large-scale flow event.

Large positive peaks were identified by selecting peaks above a certain amplitude or trigger level A_{tr}. The effect of different trigger levels was investigated for values of A_{tr} in the range σ_F to $3\sigma_F$, where σ_F is the r.m.s. value of the fixed hot-wire probe signal. The effect of the trigger level, which was found to be of second order, is described in part 2 of this study. To demonstrate the time-domain technique the value of the trigger level A_{tr} was selected as $2\sigma_F$.

The selected trigger criterion (a large positive or negative peak) is very simple to use, and it is proved in this paper that it enables the large-scale flow structure existing at a Reynolds number Re of 10^4 to be evaluated. In part 2 of this study it is demonstrated that the same criterion derives consistent large-scale flow events in the turbulent jet. The amplitude and width of the large peaks, however, vary, and a more selective trigger criterion may reveal more details of the large-scale flow structure. One possible refinement is the use of two trigger hot-wire probes A_1 and A_2 and the specification of, in addition to the signal pattern at probe A_1, a fixed phase relationship between the similar flow events occurring at probes A_1 and A_2. Other flow parameters such as a shear-stress or a vorticity component have been used as trigger criteria in other investigations, and it is possible that further details may be obtained with some of these criteria. It would be most useful if a comparative investigation of the results obtained with different trigger criteria was carried out. In doing so one must, however, remember that as the trigger criterion becomes more selective the flow processes investigated become more and more infrequent.

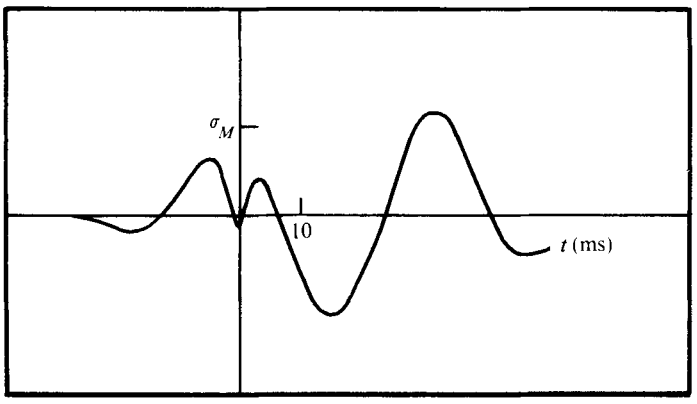

FIGURE 8. Educed signal. Moving wire: $X/D = 2{\cdot}0$; $\eta = -0{\cdot}025$.

5.2. *Eduction technique*

The basic data for the eduction technique are the time-history records of the u velocity fluctuations from the fixed (trigger) and the moving (eduction) hot-wire probes, and a pair of such time-history records is shown in figure 7. To obtain the events related to the occurrence of a positive peak in the trigger-wire signal, the time positions T_1, T_2,..., T_N of the maxima of the positive peaks above the selected trigger level $2\sigma_F$ were first evaluated by the computer. For each of these peaks, the computer then selected a particular part (t_1, t_2) of the time-history record of the eduction-wire signal which is *fixed* relative to the time position of the maximum of the positive peak (figure 7). This process was repeated for N different positive peaks in the trigger-wire velocity signal. The N individual time histories evaluated were then added together and the result divided by the number of peaks N to obtain the average or *educed* signal. The educed signal corresponding to figure 7 for $N = 250$ is shown in figure 8, demonstrating several regular peaks in the recovered signal.

This eduction method is an improved version of the eduction technique used by Lau & Fisher (1975). First, the reference time for each of the single events was selected in the present investigation as the *time* position of the maximum of the positive peak in the signal from the fixed hot-wire probe (figure 7). In the method of Lau & Fisher a trigger event occurred each time a pre-set trigger level was reached, therefore the reference time for each separate event was the intersection between the part of the peak with positive slope and the trigger level, and not the position of the peak maximum. Second, a Hewlett Packard 3721A correlator was used by Lau & Fisher in the repetitive signal mode, to obtain their educed signals. The correlator is, however, capable of evaluating only positive time events. By using a digital computer for the data reduction, both positive and negative values for t_1 and t_2 (figure 7) could be selected in this study. This enabled the investigation of flow processes both upstream and downstream of the fixed-wire position, as described in § 6 of this paper.

As mentioned in the introduction, the initial part of this investigation was aimed at increasing the amplitude of the educed signals. In the method used by Lau & Fisher (1975) the educed signals were very small, the maximum amplitude u_p of the

recovered signals often being less than 10–20 % of the r.m.s. value σ_M of the eduction-wire signal. To improve the eduction technique, it was therefore originally considered important to recover a significant amount of the eduction-wire signal. To illustrate this point it is useful to discuss the principle behind the eduction technique, as put forward by Lau & Fisher.

If we consider the signal $V(t)$ from the eduction wire relative to a specific event in the trigger-wire signal, then the signal $V(t)$ can be assumed to be the sum of two components $A(t)+B(t)$, where $A(t)$ represents the part which is related to the specified event in the trigger-wire signal and $B(t)$ corresponds to the random local flow events. For N separate events we therefore obtain

$$\begin{aligned} V_1(t) &= A(t)+B_1(t), \\ V_2(t) &= A(t)+B_2(t), \\ &\vdots \\ V_N(t) &= A(t)+B_N(t). \end{aligned}$$

As the local event $B(t)$ is assumed to be a random function, it follows for large values of N that

$$\frac{1}{N}\sum_{k=1}^{N} B(t) \to 0 \quad \text{for} \quad N \to \infty.$$

For large values of N the average or educed signal therefore becomes

$$\frac{1}{N}\sum_{k=1}^{N} V(t) \cong A(t)$$

with $A(t)$ the part of the velocity which is related to the selected flow event at the trigger-wire position.

The amplitude of the signal recovered by Lau & Fisher was, however, so small that this simplified interpretation cannot be valid. The eduction principle illustrated in figure 7 and the corresponding educed signal in figure 8 demonstrate the deviation from the interpretation proposed by Lau & Fisher. Several distinct positive and negative peaks can be observed in the educed signal in figure 8. If we look at the three separate time-history events (t_1, t_2) in figure 7, then corresponding peaks can be identified in the three separate events. A considerable variation is, however, seen to exist in both the amplitude and the relative position of the individual peaks, and as a result of the averaging procedure in the eduction technique the magnitude of the regular peaks in the educed signal will usually be smaller than that of the peaks in the separate events. *In most cases it is therefore not possible directly to relate the magnitude of the educed signal to the 'average' large-scale flow events,* as suggested by Lau & Fisher.

The maximum amplitude of the educed signal at the moderate Reynolds number of 10^4 was found to be almost an order of magnitude larger than the results obtained by Lau & Fisher for the turbulent jet as shown in figure 9. The large-scale flow structure at moderate Reynolds number is known (§4) to be very coherent, which explains the large amplitude of the recovered signal, while the small signal recovered in the turbulent case is due to a much smaller spatial coherence of the flow structure related to the selected trigger event, and not to imperfections in the eduction technique as suggested by Lau & Fisher. This is consistent with the present results for the

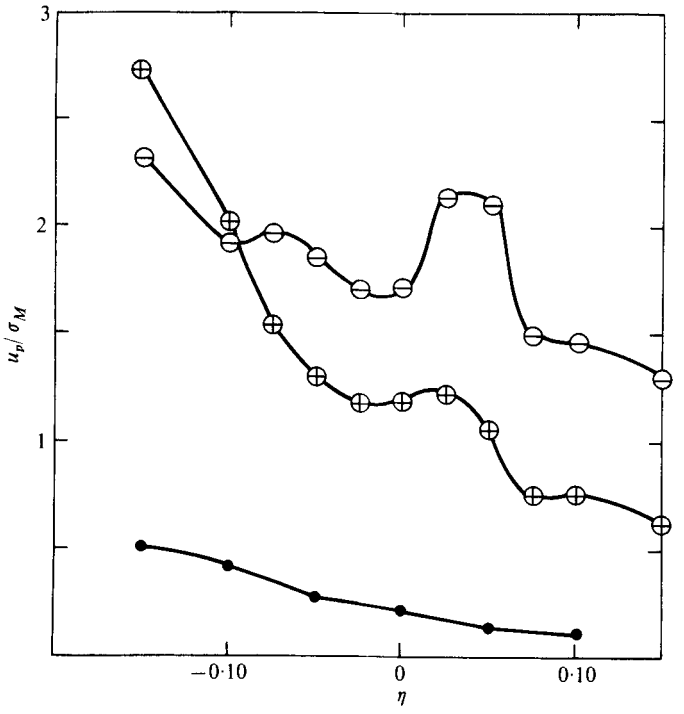

FIGURE 9. Maximum amplitude of positive and negative educed signals at $X/D = 2{\cdot}0$. Fixed wire: $\eta = -0{\cdot}15$. $Re = 10^4$. ●, maximum amplitude of negative educed signals at $X/D = 2{\cdot}5$ with fixed wire at $X/D = 2{\cdot}0$, $\eta = -0{\cdot}05$ for $Re = 2 \times 10^5$ (Lau & Fisher 1975).

turbulent jet (part 2), where the improvement in the eduction technique produced only a small increase in the amplitude of the educed signals.

Two vital types of information are, however, retained in the educed signal. First, the basic shape of the time history is maintained, making identification of positive and negative peaks possible. Second, although a small variation in the relative time position of the individual peaks occurred between the separate events, averaging over a large number of events N ensures that the *time* position of the peak in the educed signal is equal to the *time* position of the corresponding *average* large-scale flow event. To transform this time information into the corresponding large-scale flow events a new signal interpretation method was developed.

5.3. *Signal interpretation method*

To transform the time-history information in the educed signals into the large-scale flow events, a method which identifies the related peaks in time and space was developed.

The mean jet flow is in the axial direction. However, as the width of the mixing layer increases with axial distance it was decided to look at the development of the peaks along constant-η lines. Plotting the educed signals for constant-η lines on linear X/D, t graphs, as shown in § 6, enables the determination of the time and space relationship for the regular peaks. By identifying the similar events along all the η lines the large-scale flow structure can be evaluated, as demonstrated in § 7.

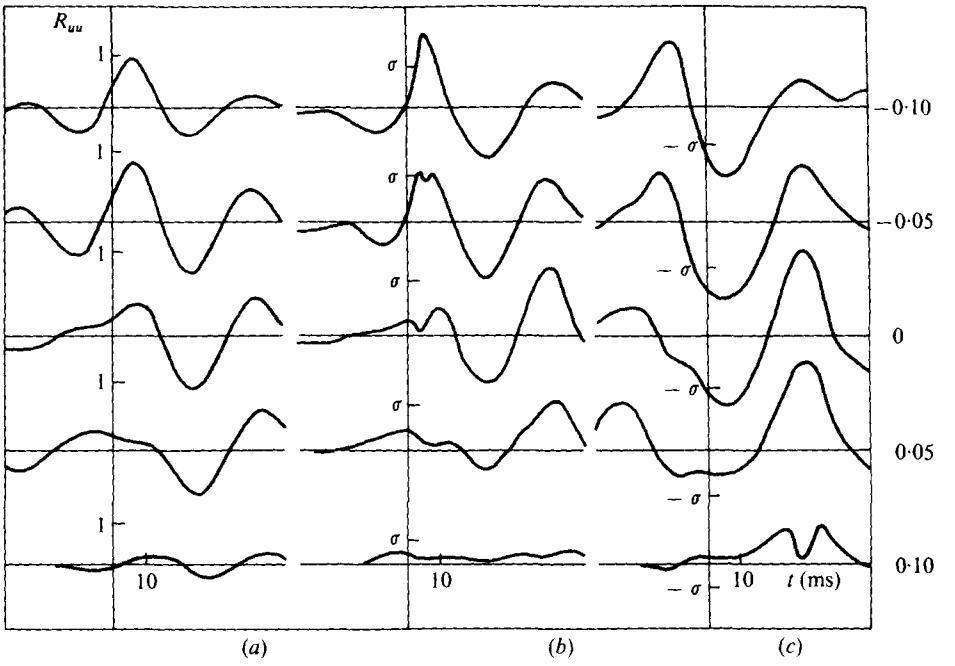

FIGURE 10. Comparison of cross-correlation and positive and negative educed signals at various radial positions at $X/D = 2{\cdot}25$. Fixed wire: $X/D = 2{\cdot}0$, $\eta = -0{\cdot}15$. $Re = 10^4$. (*a*) Correlation. (*b*) Positive eduction. (*c*) Negative eduction.

Cross-correlation techniques have been used for a long time to infer flow structures, and it is useful to compare corresponding cross-correlations and educed signals to demonstrate the limitations of cross-correlation techniques.

5.4. *Comparison of cross-correlations and educed signals*

The signals obtained from a fixed hot-wire probe at $X/D = 2{\cdot}0$, $\eta = -0{\cdot}15$ and a hot-wire probe traversed radially at $X/D = 2{\cdot}25$ were chosen for the comparison. At each of the selected radial positions the cross-correlation coefficient R_{uu} and the corresponding educed signals obtained using both large positive and large negative peaks as trigger criteria were evaluated, and the results are plotted in figure 10. A comparison of the positive and negative educed signals shows a clear difference between the regular signal pattern in the two cases. The positive and negative trigger criteria therefore select different large-scale flow events.

The eduction technique involves an addition procedure, and the basic shape of the original time-history record is therefore retained. As correlation techniques are based on a multiplication, the most significant peak will be a positive peak regardless of the type of event which contributed most to the correlation. Furthermore, correlation techniques use a continuous time record and consequently integrate over all flow events. Correlation techniques therefore cannot extract separate flow events like, for example, the double peaks occurring in the positive educed signal in the middle of the mixing region.

Another very significant difference between the results obtained by eduction and correlation techniques can be observed in the convection velocities evaluated.

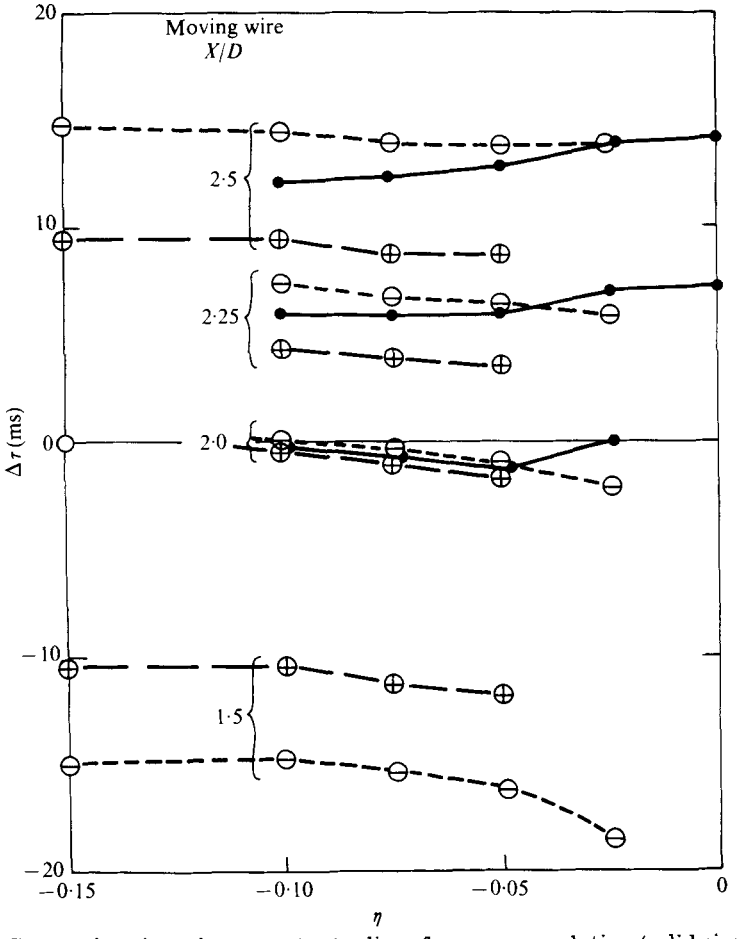

FIGURE 11. Convection time along constant-η lines for cross-correlation (solid circles) and positive and negative educed signals. Fixed wire: $X/D = 2{\cdot}0$, $\eta = -0{\cdot}15$. $Re = 10^4$.

5.4.1. *Convection velocity.* Many different definitions have been suggested for the 'convection velocity', but to demonstrate the difference between results obtained by correlation and eduction techniques it is sufficient to select the following definition: the development of the correlation or educed signal is followed along a constant-η line and we *define* the convection velocity as

$$U_c = [\Delta X/\Delta t]_{\eta=\text{const}}, \tag{2}$$

where ΔX is the axial separation between two selected points on the η line and Δt is the time interval between the most significant peaks in the correlation or educed signals at the two points.

The time positions $\Delta\tau$ for the most significant peak in the correlation and educed signals in the flow region, $1{\cdot}5 \leqslant X/D \leqslant 2{\cdot}5$, $-0{\cdot}15 \leqslant \eta \leqslant 0$, have been evaluated and are plotted in figure 11. The convection time between two axial stations is seen to be much smaller for positive eduction than for negative eduction, and the corre-

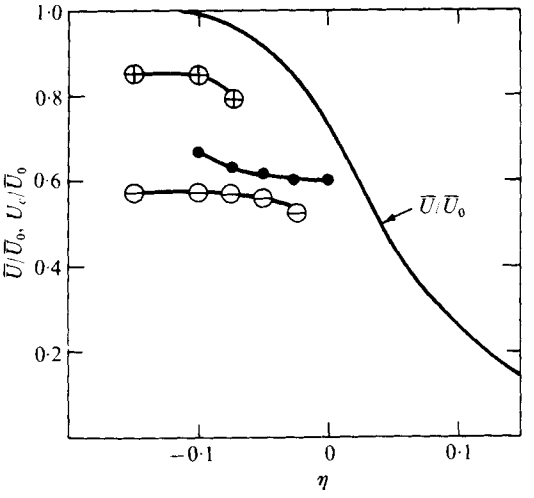

FIGURE 12. Mean velocity profile and convection velocity of cross-correlation (solid circles) and positive and negative educed signals at $X/D = 2{\cdot}0$. $Re = 10^4$.

sponding convection velocities, plotted in figure 12, demonstrate that there is a distinct relationship between positive eduction and a fast-moving large-scale flow event. Similarly negative eduction is shown to be related to a slow-moving part of the flow. The correlation technique integrates over all flow events and therefore evaluates an 'average' convection velocity. When the moving wire is close to the fixed wire, the correlation is dominated by the large amplitude part of the signal, and we observe in this case that the correlation convection velocity is nearly the average value of the positive and negative educed convection velocities. It will be shown in part 2 that the 'difference' between the positive and negative educed convection velocities is related to the deformation rate of the large-scale flow structure; correlation techniques completely fail to determine this aspect of the flow structure.

However, the 'convection velocity' concept is unnecessary for the evaluation of the large-scale flow structure, and it will not be discussed further in this paper.

6. Eduction results

Eduction measurements were carried out in the flow region $0{\cdot}75 \leqslant X/D \leqslant 2{\cdot}5$, $-0{\cdot}15 \leqslant \eta \leqslant 0{\cdot}15$ for a moderate nozzle Reynolds number of 10^4. The fixed hot-wire probe was placed at $X/D = 2{\cdot}0$, $\eta = -0{\cdot}15$ and the measuring points of the moving hot-wire probe were selected along constant-η lines, as shown in figure 1. Eductions were carried out using both positive and negative peaks as trigger criteria. For clarity only the results obtained using triggering of positive peaks are presented in this paper.

To relate the temporal and spatial variation of the regular peaks in the educed signals, their development along constant-η lines was studied. If we look at a typical educed signal like the one in figure 8, then several positive and negative peaks can be identified in the signal. However, when the amplitude of the peak is small it

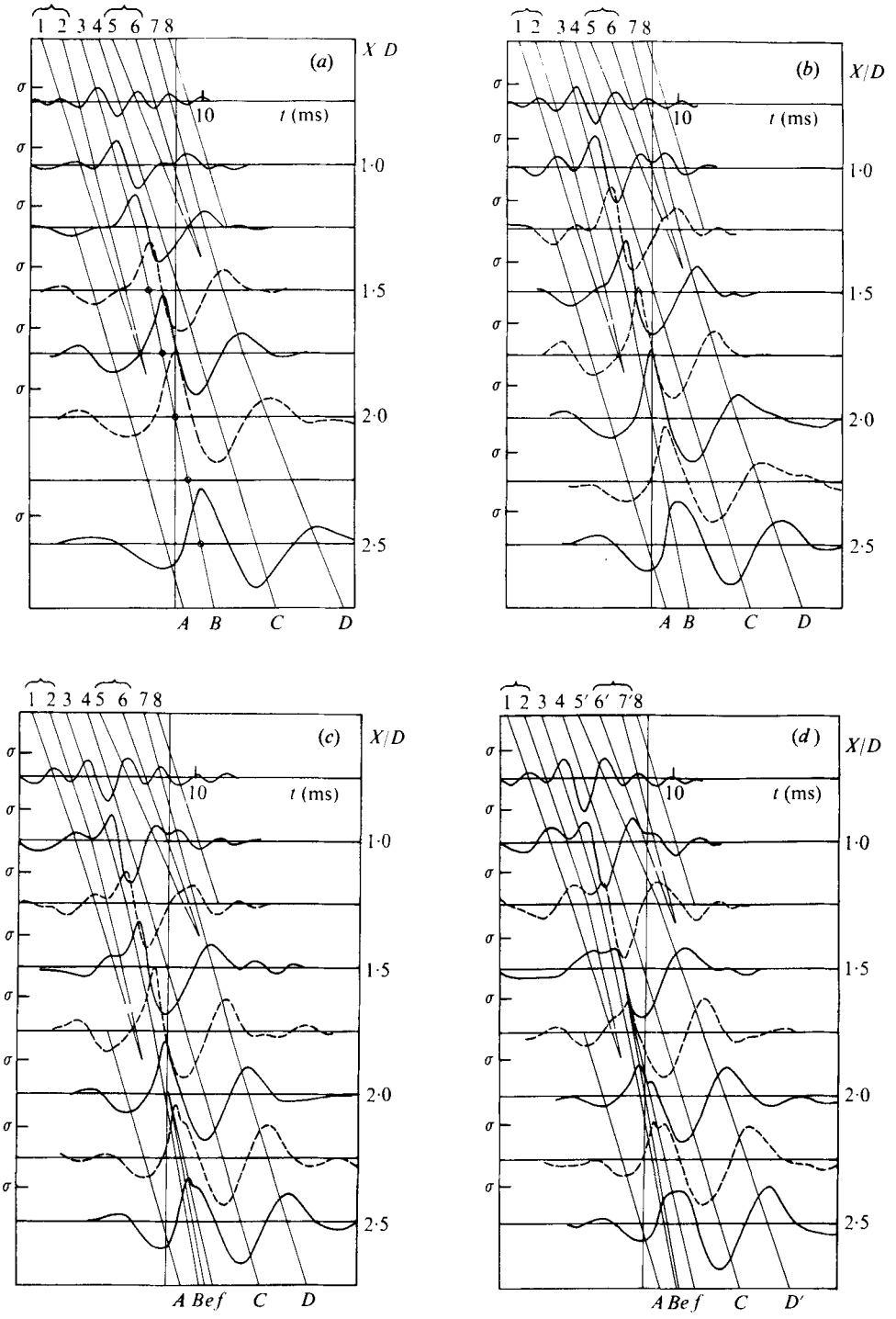

FIGURES 13(*a–d*). For legend see p. 660.

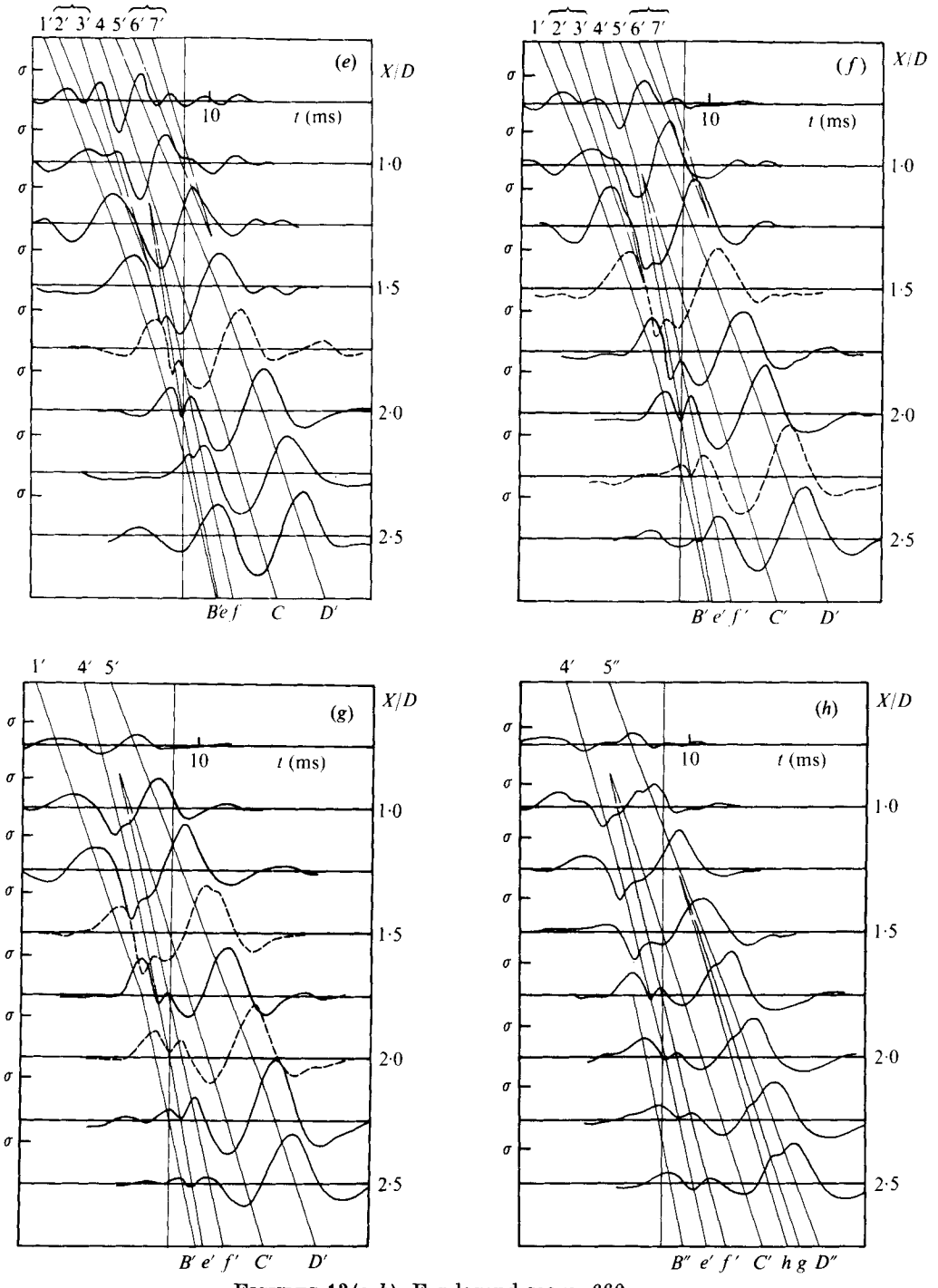

FIGURES 13(*e*–*h*). For legend see p. 660.

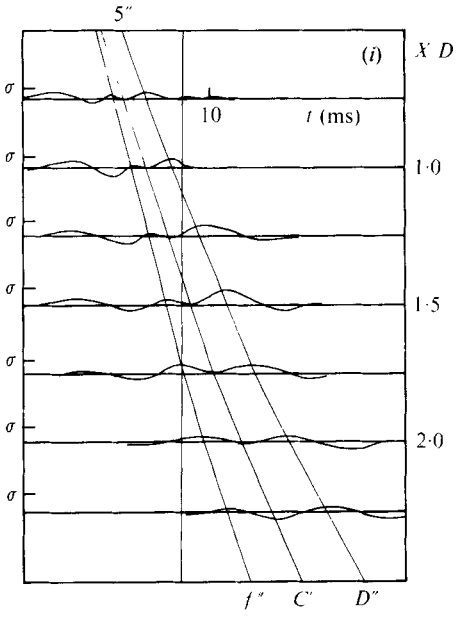

FIGURE 13. Axial development of positive educed signal along (*a*) $\eta = -0{\cdot}15$, (*b*) $\eta = -0{\cdot}10$, (*c*) $\eta = -0{\cdot}075$, (*d*) $\eta = -0{\cdot}05$, (*e*) $\eta = -0{\cdot}025$, (*f*) $\eta = 0$, (*g*) $\eta = 0{\cdot}025$, (*h*) $\eta = 0{\cdot}05$ and (*i*) $\eta = 0{\cdot}15$.

becomes necessary to determine whether the peak is 'regular' (i.e. related to a large-scale flow event) or a random occurrence caused by the data processing of a particular time-history record. To solve this problem it was necessary to look at the educed signals from neighbouring points. Studying the educed signals it was concluded that a 'regular' peak (corresponding to a large-scale flow event) could be identified only when the following *minimum* criteria were satisfied:

(i) The peak must develop regularly between a minimum of three consecutive points on an η line.

(ii) A similar type of peak must be identifiable at a minimum of two consecutive η lines.

Thus, having defined a 'regular' peak, we can now proceed with the identification of all the regular peaks and their corresponding large-scale flow events.

It proved very instructive to plot the educed signals for a constant value of η on a linear X/D, t graph. The corresponding eduction graphs for the different η lines are shown in figures 13(*a*)–(*i*). To facilitate the evaluation of the time and space relationship of the regular events, the time positions for each type of regular peak have been linked on all the graphs. Notice that these curves are not always straight lines and that acceleration and deceleration effects can therefore be derived by the time-domain technique.

Having measured all the educed signals, we must now identify the separate flow events which correspond to these regular peaks and their spatial and temporal development. To do so it is necessary (*a*) to study the development of the regular peaks along constant-η lines and (*b*) to identify the related events for the different values of η.

As the trigger wire was placed on the line $\eta = -0{\cdot}15$, this line was considered first. At this stage we cannot translate the regular peaks into the corresponding large-scale flow events. Instead it proved useful to label the regular peaks occurring in the educed signal at the larger values of X/D as A–D and to identify the regular peaks in the educed signal close to the nozzle ($X/D = 0{\cdot}75$) as 1–8 (figure 13*a*).

In §5 it was demonstrated that it is not possible directly to relate the amplitude of the educed signals to the velocities occurring in the average large-scale flow structure. The amplitude information contained in the educed signals (figures 13*a*–*i*) will therefore not be discussed in this paper. We shall concentrate instead on the temporal and spatial relationship of the regular large-scale flow events.

The trigger criterion was selected as a large positive peak at the point $X/D = 2{\cdot}0$, $\eta = -0{\cdot}15$, and the corresponding peak event has been labelled B in figure 13(*a*). The figure shows that a flow event B corresponding to the curve $B/3$ can be identified at all values of X/D. If we consider the other regular flow events relative to the flow event $B(t_B(X))$, then events which follow flow event B occur in the time domain $t(X) > t_B(X)$ while events which precede flow event B are observed for $t(X) < t_B(X)$.

A regular flow event C corresponding to a negative peak follows event B and can be recognized as the curve $C/4$ at all axial positions. No additional large-scale flow events can be identified between flow events B and C at any axial position. However, on either side of events B and C similar peak developments are seen to occur close to the jet exit. Two sets of regular positive and negative peaks 1, 2 and 5, 6 exist close to the nozzle ($X/D = 0{\cdot}75$). As the flow progresses downstream the amplitude of the peaks decreases, and the peaks disappear in the axial region of $X/D = 1{\cdot}3$–$1{\cdot}8$.

In §8 it is demonstrated that the *disappearance* of these peaks is related to the *coalescence* of two vortices. Peak events 5 and 6 are followed by a regular positive peak event $D/7$, which can be identified at all the axial positions, and a negative peak event 8 identifiable only close to the nozzle exit.

At the larger values of X/D a negative peak event A is seen to precede flow event B. However, flow event A cannot be identified close to the nozzle because its initial development is not sufficiently regular in time and space relative to the occurrence of the trigger event B.

To evaluate the spatial extent of the regular flow events in the mixing region, we must determine the related events on the different η lines. This identification of the flow events was obtained by comparing the graphs in figures 13(*a*)–(*i*) for consecutive values of η, using the identified events on the line $\eta = -0{\cdot}15$ (figure 13*a*) as the initial references.

On comparing figures 13(*a*) and (*b*) it is clear that the same number of regular flow events can be identified on both graphs. The time positions of corresponding peaks on the two graphs, however, occur at slightly different times, producing a different time and space relationship for the similar flow events on the two graphs. This variation in the time and space relationship for related flow events occurs throughout the mixing region and it has a direct relationship with the large-scale flow structure as discussed in § 7.

When the moving hot-wire probe enters the mixing region ($\eta = -0{\cdot}075$) all the initial events A–D/1–8 can still be identified on the graph (figure 13*c*). A new set of

peaks (e, f), however, appears between flow events B and C at the larger values of X/D. (New peaks are denoted by small letters.) It will be shown in the next graphs that peak events e and f can be identified closer to the nozzle when $\eta > -0{\cdot}075$. The existence of events e and f in figure 13(c) only at large values of X/D is therefore due either (i) to events e and f growing in size as they move downstream or (ii) to an inward movement of a flow structure of fixed size intersecting the line $\eta = -0{\cdot}075$ at $X/D = 2$. It will be shown in § 7 that the first interpretation is the correct one.

As we move further out in the mixing region a steady change occurs in the educed signals. To identify the related events at the new values of η, the events at each value of η were compared with the regular events at the preceding value of η. For clarity we shall therefore discuss only the *change* in the *type* of regular event at each new value of η.

A different coalescence related to peaks 5, 6 and 7 occurs at $\eta = -0{\cdot}05$ (figure 13d), and these peaks have consequently been identified as 5′, 6′ and 7′. (A dash is used to differentiate between similar types of peaks at small or large values of X/D which have different spatial developments.) The peak disappearance or coalescence is seen to involve peaks 6′ and 7′ and the regular positive peak following flow event $C/4$ now corresponds to curve $D'/5'$ instead of to curve $D/7$ as in figures 13(a)–(c). The peak pair (B, e) is also observed to disappear between $X/D = 2{\cdot}75$ and $3{\cdot}0$.

At $\eta = -0{\cdot}025$ (figure 13e) a new coalescence process corresponding to the peaks 1′, 2′ and 3′ occurs. The peak disappearance now involves peaks 2′ and 3′ and the trigger event $B/3$ is replaced by a different event $B'/1'$. Furthermore the negative peaks corresponding to flow events A and 8 are now so irregular that there is no justification for identifying A and 8 as regular flow events on this graph.

Figure 13(f), for the middle of the mixing region ($\eta = 0$), shows a new development for peaks C', e', f' and 4′. Flow event C', corresponding to a regular negative peak at large values of X/D, is now seen to merge with flow event f' at small values of X/D, while the large negative peak 4′ at $X/D = 0{\cdot}75$ has become related to curve $e'/4'$.

No new peak development occurs at $\eta = 0{\cdot}025$ (figure 13g), but the two pairs of coalescing peaks 2′, 3′ and 6′, 7′ cannot be identified in the educed signals at this or larger values of η.

The regular event $B'/1'$ has disappeared together with peak 1′ at $\eta = 0{\cdot}05$ (figure 13h). A much less regular event B'' can be observed at the larger values of X/D, but the origin of this type of event cannot be evaluated from the educed signals. A new pair of peak events (h, g) is also observed for the first time between events C' and $D''/5''$.

The flow events which could be identified in the educed signals at $\eta = 0{\cdot}075$ and $0{\cdot}10$ were the same as those occurring at $\eta = 0{\cdot}05$, except that the positive peak corresponding to event B'' is so irregular at $\eta = 0{\cdot}10$ that it cannot be described as a regular flow event, and the corresponding figures have consequently been omitted.

At the outer edge of the mixing layer $\eta = 0{\cdot}15$ (figure 13i) only flow events f'', C' and $D''/5''$ remain.

Having identified the regular large-scale flow events throughout the mixing region, and with the time and space curves for these events drawn on all the graphs, we can now derive the large-scale flow structure in the mixing region of the jet flow.

7. Average large-scale flow structure

A large-scale flow event is continuous and identifiable over a significant part of the mixing-layer width, and it was found useful to describe the spatial curve which relates all the points of a particular flow event (e.g. event A) at a given time as an event *front*.

The large-scale flow events have been identified from measurements of the u velocity component. However a radial velocity component v also exists, often occurring in phase with the u velocity fluctuations, as described in § 8 of this paper. Therefore, when we follow the development of a flow event along a constant-η line, we do *not* follow the progression of a given or fixed part of the flow structure, but we detect the *intersection* in time of the event 'front' as it passes the measuring points. The time-domain technique thus enables us to determine, at any given time, the spatial position of the related events on the event 'fronts' from the eduction graphs (figures 13*a–i*). In this section we shall evaluate the spatial position of *all* the regular event 'fronts' at selected times.

The derivation of the event 'fronts' is based on measurements along constant-η lines, but from the above discussion it is clear that the spatial positions of the event 'fronts' could also have been obtained by following the peak developments along constant-Y lines or any other type of curve which extends continuously in the axial direction.

In this investigation the origin of the time scale for the educed signals plotted in figures 13(*a*)–(*i*) was selected as the occurrence of the trigger event B at the fixed-wire position $X/D = 2{\cdot}0$, $\eta = -0{\cdot}15$. The corresponding time and space relationship $t_B(X/D)$ for the trigger event B is plotted in figure 13(*a*).

For each value of t_B it is possible to derive the corresponding spatial position of the large-scale flow structure as discussed below. Flow events which just precede or follow the trigger event B have the greatest regularity relative to the flow event B, and to demonstrate the spatial development of the large-scale flow structure we have therefore restricted the reference times $t_B(X/D)$ to the values $X/D(B) = 1{\cdot}5$, $1{\cdot}75$, $2{\cdot}0$, $2{\cdot}25$ and $2{\cdot}5$, marked with circles on figure 13(*a*). These reference times enabled all the regular flow events to be evaluated except the peak coalescence (1, 2). However, as a similar coalescence occurs for the peak pairs (1, 2) and (5, 6), all types of flow event are considered, and the reference time can if necessary be extended to obtain the spatial development of the coalescence process (1, 2).

The spatial positions of the related large-scale flow events (event 'fronts') were evaluated in the following way for each of the selected reference times. On the eduction graphs (figures 13*a–i*) we have determined the relationship between the time and the axial position of all the regular flow events. Therefore, when the reference time t_B is specified the axial position of the event can be found, and as the event progresses along a constant-η line the *spatial* position of the point is also known. Let us illustrate this for the reference time $t_B(X/D = 1{\cdot}5)$. On figure 13(*a*) ($\eta = -0{\cdot}15$) we can determine the corresponding axial positions of events A, B, C, 5 and 6, and the spatial positions of these points on the line $\eta = -0{\cdot}15$ have been plotted on the top graph in figure 14. Events A, B, C, 5 and 6 can also be identified on figures 13(*b*) and (*c*) and the spatial positions of these events on the lines $\eta = -0{\cdot}10$ and $-0{\cdot}075$ are also plotted on the top graph in figure 14. Near the centre of the mixing layer ($\eta = -0{\cdot}025$) flow events e and f can also be identified, and by evaluating the

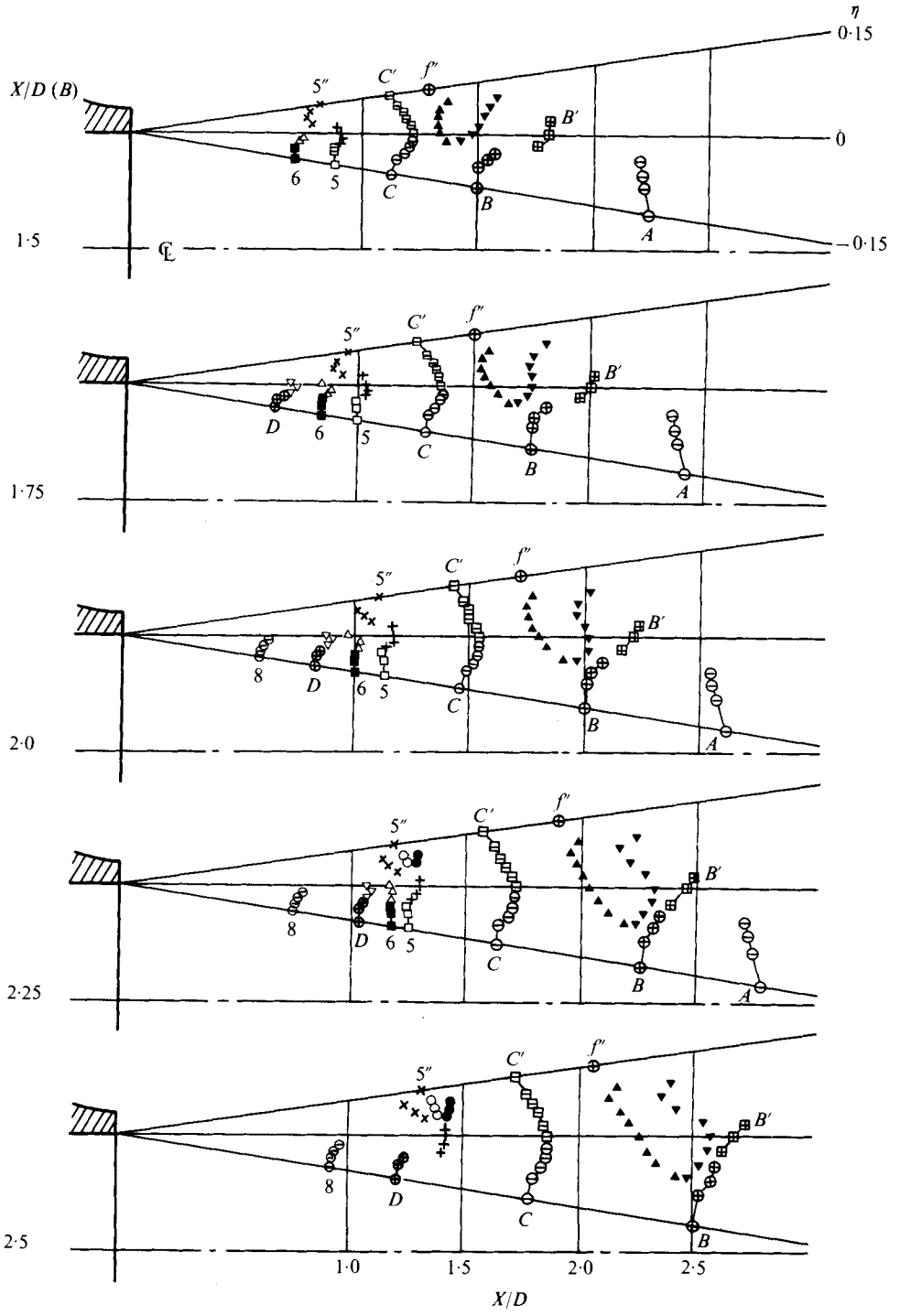

FIGURE 14. Axial development of the large-scale structure in the mixing region of a round free jet. $Re = 10^4$. +, 5′; ▼, e/e'; ▲, f/f'; △, 6′; ▽, 7′; ○, g; ●, h.

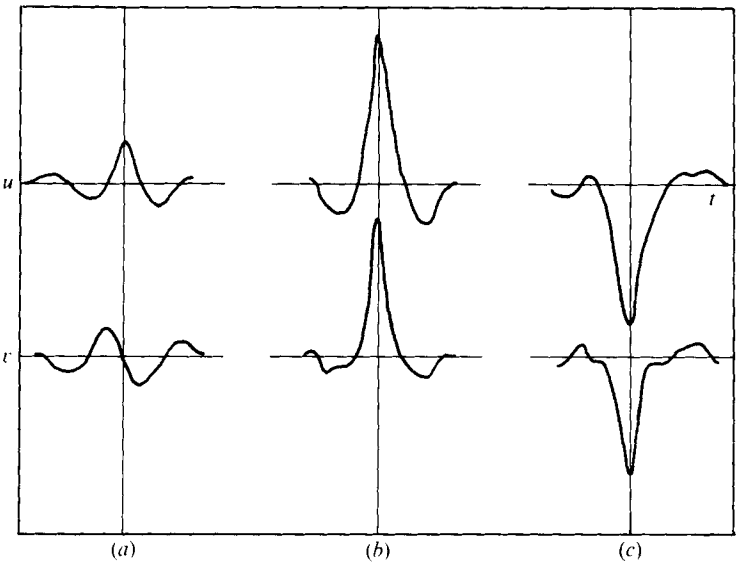

FIGURE 15. Phase relationship between u and v velocity components for (a) fast-moving potential-core flow, (b) ejection of potential-core fluid and (c) entrainment of surrounding still air.

regular flow events line by line we obtain the complete spatial distribution of all the average large-scale event 'fronts' at the reference time $t_B(X/D = 1{\cdot}5)$ as shown in the top graph in figure 14.

The eduction measurements were limited to the axial region $0{\cdot}75 \leqslant X/D \leqslant 2{\cdot}5$. It was found that the corresponding time and space relationship for the regular flow events could be determined accurately only in the axial region $0{\cdot}5 \leqslant X/D \leqslant 2{\cdot}75$. Flow events occurring outside this axial region are therefore not included on figure 14. By extending the measurement region closer to the nozzle ($X/D < 0{\cdot}75$) and further downstream, a complete spatial development of the flow events can be obtained. However, no new type of flow event occurs outside the axial region $0{\cdot}5 \leqslant X/D \leqslant 2{\cdot}75$, and for reasons of time the measurement region was not extended.

By repeating the evaluation of the large-scale flow structure for all the selected reference times, the temporal and spatial developments of the large-scale event 'fronts' were obtained as shown in figure 14.

8. Identification of separate flow events

Having derived the large-scale event 'fronts' there only remains to interpret these in terms of the corresponding flow events, and to demonstrate the agreement between the flow-visualization and educed large-scale flow structure.

It is possible to interpret several of the event 'fronts' directly from the measured axial velocity component, but simultaneous measurements of the u and v components greatly facilitate the interpretation of the event 'fronts' in figure 14. It is shown in part 2 that a given phase relationship exists between the u and v component for each type of flow event, and typical examples are shown in figure 15 for (a) fast-moving potential-core flow, (b) ejection of potential-core fluid and (c) entrainment of surrounding still air.

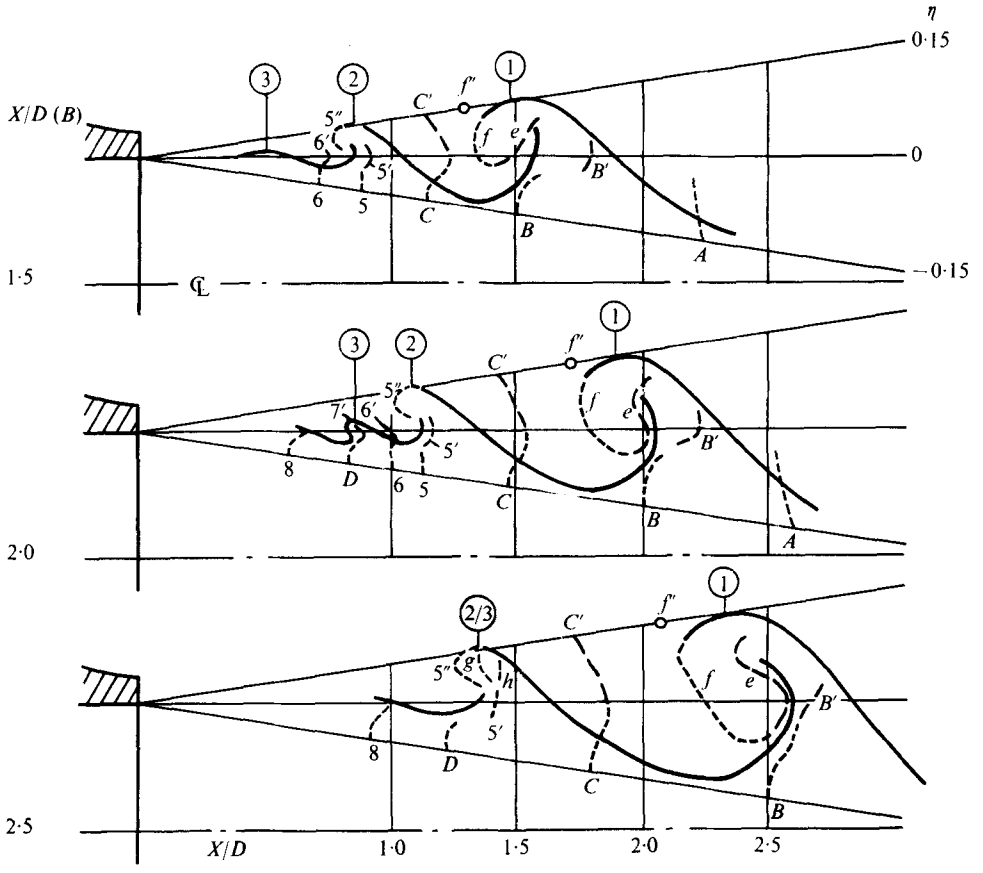

FIGURE 16. Comparison of educed large-scale structure and flow-visualization structure.

Owing to time limitations, it was not possible to extend part 1 of this investigation to include v-component measurements, and we shall instead discuss the individual flow events after we have compared the flow-visualization and educed large-scale flow structure.

On comparing the educed structure (figure 14) and figures 6(*a*)–(*c*), it is clear that the observed vortex corresponding to the trigger event B is represented by the vortex outline e/f. The spatial position of the vortex structures corresponding to events $5'/5''$ and $7'$ also agrees with the average flow-visualization results when we take into account the fact that the flash bulb was triggered when the signal reached the trigger level, so that the flow-visualization pictures correspond to a slightly earlier time than the educed flow structure (figure 14), which was derived from the time positions of the peak maxima.

The flow-visualization pictures provided clear evidence of the average separation curve between the nozzle air flow and the entrainment flow, a feature which was not clearly identified by the present time-domain technique. These average separation curves are drawn as heavy lines on the comparative graphs in figure 16. This figure proves the identity of the large-scale flow structures (fixed relative to trigger event B)

observed by flow visualization and derived by the new time-domain technique. Further details may be obtained by improvements in the time-domain technique, but the basic agreement between the flow-visualization results and the educed large-scale flow structure have been proved in figure 16. The comparison of the flow-visualization and educed flow structure (figure 16) enables the identification and interpretation of the separate regular flow events, which are fixed relative to the occurrence of the selected trigger event B.

Three separate vortex structures 1, 2 and 3 can be identified on figure 16, and it is demonstrated in this section that vortex structure 1 is the result of a single vortex-pairing close to the nozzle. The figure demonstrates that the time-domain technique has derived most of the significant large-scale flow events:

(i) The spatial relationship between the induced fluctuations in the potential core and the large-scale flow structure in the mixing region of the jet.

(ii) The flow paths for the ejection of the fast-moving potential-core fluid into the vortex structures.

(iii) The entrainment of fluid from the surrounding still air behind the vortex structures.

(iv) The spatial growth of the vortex structure 1 corresponding to the selected trigger event.

(v) The timewise variation of the spatial separation between vortex structures 1, 2 and 3.

(vi) The coalescence of vortex structures 2 and 3, which follow vortex structure 1.

For flow events in the potential core close to vortex structure 1, there is a clear relationship between the fast-moving fluid and positive peaks (event B) and between slow-moving fluid and negative peaks (events A and C). The distance between C and B is consequently seen to increase and the distance between B and A to decrease as the flow moves downstream.

The axial development of vortex structures 2 and 3 involves large radial movements, because vortex structure 3 moves inside vortex structure 2 as they coalesce into one big vortex structure at $X/D = 1{\cdot}5$. The related flow events 5, 6 and D correspond to the *intersection* of these event 'fronts' with the constant-η lines, and when large radial movements occur there is not always a direct relationship between the peak signature and the *axial* velocity of the event front, as can be seen from the signature of events 5 and 6.

Figure 16 demonstrates that flow events 5, 6 and D, 8 are related spatially respectively to vortices 2 and 3 as flow events B and C are to vortex 1. Vortex 3 moves inside vortex 2, and their coalescence into one large vortex structure corresponds to the disappearance of flow events 5 and 6 at $X/D \simeq 1{\cdot}3$. The remaining positive and negative peaks events D and 8 correspond to fast- and slow-moving parts of the fluid in a way similar to flow events B and C for vortex 1. All the flow events evaluated travel with different speeds, and the new time-domain technique has therefore derived the nonlinear development of the large-scale flow structure.

Flow event C is difficult to interpret in the inner part of the mixing region ($\eta < 0$). The spatial curve which separates the nozzle flow C and the entrainment flow C' varies between separate vortex structures, and measurements in this region therefore contain contributions from both types of event. In the outer part of the mixing layer the flow path C' for the entrainment fluid is clearly defined. It will be demonstrated

in part 2 of this study that, when the trigger wire is placed in the middle of the mixing region ($\eta = 0$) then the flow path C' can also be identified in the inner part of the mixing region ($\eta < 0$), and that in this region the entrainment flow path C' differs from the curve C derived in this paper.

In the outer part of the mixing region ($\eta > 0$) a strong relationship exists between the entrainment path C' and the outline f' of vortex structure 1 as they merge close to the nozzle (figures 13*f–j*). As shown in the following, flow events C' and f' are related to the formation of vortex 1 by a single vortex-pairing process close to the nozzle. A similar relationship does not exist between flow events C and f (figures 13*c–e*), and the merging of events e and f towards the nozzle is due to the radial growth of vortex 1. As mentioned earlier, the entrainment path C' can be identified in the inner part of the mixing layer, extending the relationship between C' and f' to this region. It is therefore unnecessary to distinguish between flow events f and f' and e and e', and the single symbols e and f have been used on figure 16.

Only potential-core flow events (A, B, C, D, 5, 6 and 8) occur along the line $\eta = -0{\cdot}15$. As we move into the mixing region these events remain identifiable until $\eta \simeq -0{\cdot}05$, but a hot-wire probe placed in this region ($-0{\cdot}15 < \eta < -0{\cdot}05$) also records the entrainment of fluid from the surrounding still air. (The entrainment paths C' and 6′ in the inner part of the mixing region can be obtained by placing the fixed hot-wire probe at $\eta = 0$.)

At $-0{\cdot}05 \lesssim \eta \lesssim -0{\cdot}025$ we observe for the first time the flow processes occurring in vortex structures 1, 2 and 3. The ejection path for the fast-moving potential-core fluid into vortex structure 1 is given by curve B' and the corresponding ejection paths for vortex structures 2 and 3 are respectively curves 5′ and 7′. Vortex structure 1 is the result of a single vortex-pairing process preceding the pairing of vortices 2 and 3, and the axial jump between B and B' (at $t_B(X/D = 1{\cdot}5)$) is similar to the axial jump between D and 5′ at $t_B(X/D = 2{\cdot}5)$ caused by the disappearance of the potential-core flow events 5 and 6. As the vortex structure 1 progresses downstream the potential-core event B travels faster than the ejection path B', and the two events are seen to link up at $X/D \simeq 2{\cdot}5$.

The outline of vortex 1 is given by curves e and f, and a highly nonlinear development of the vortex is observed as it moves downstream. Curves B' and f' were shown in figures 13(*d*)–(*f*) to merge downstream, therefore vortex structure 1 separates from the potential-core fluid at $X/D \simeq 3{\cdot}0$.

The spatial separations of vortex structures 1, 2 and 3 at the three selected times are shown in figure 16, and the graphs demonstrate that the three vortices travel at different speeds.

Separate flow events in vortex structure 2 and the coalescence of vortices 2 and 3 into a single large vortex have also been derived by the time-domain technique. At the reference time $t_B(X/D = 1{\cdot}5)$ curve 5′ is the ejection path for the potential-core fluid into vortex structure 2, curve 5″ the outline of vortex 2 corresponding to curve f for vortex 1, and curve 6′ is the entrainment path behind vortex 2. The position of vortex 3 is given by the potential-core event D and the ejection path 7′. Vortex 3 is however small, and as it is also quite remote in space and time from the fixed hot-wire probe at $X/D = 2{\cdot}0$, it was not possible to derive the other feature of vortex 3 in the mixing region. (Details of vortex 3 can be obtained by placing the fixed hot-wire probe closer to the nozzle).

The coalescence of vortices 2 and 3 may be clearly identified from figures 14 and 16. Vortex 3 progresses much faster than vortex 2 and moves inside vortex 2. Vortices 2 and 3 coalesce into a new large vortex, which subsequently develops several regular features like vortex 1. The events 5, 6 and 5′, 6′ disappear at $X/D \simeq 1{\cdot}3$, while the potential-core events D and 8 related to vortex 3 and the ejection path 5′ for vortex 2 are retained. Curve 5″ develops into the outline of the combined vortex 2/3 and two new regular vortex features g and h are seen to emerge from the coalescence process.

By extending the reference time backwards to values $t_B < t_B(X/D = 1{\cdot}5)$, it is easy to demonstrate from figures 13(*a*)–(*i*) that vortex 1 is the result of a vortex-pairing process similar to the vortex pairing 2/3. The final stage of this coalescence process is clearly visible at $X/D \simeq 1{\cdot}5$ in figure 6(*a*). The coalescence of vortices 2 and 3 has been shown to correspond to the educed peak signature (5 (> 0), 6 (< 0), D (> 0), 8 (< 0)) with the peak pair (5, 6) disappearing as the flow progresses downstream. A similar peak signature (1 (> 0), 2 (< 0), B (> 0), C (< 0)) exists for vortex 1 with the peak pair (1, 2) disappearing. Although the flow processes for the two vortex pairings are similar, differences can be observed from figures 13(*a*)–(*i*). The potential-core coalescence length for vortex 1 ($X/D \simeq 1{\cdot}8$) is longer than the coalescence length ($X/D \simeq 1{\cdot}4$) for the vortex pairing 2/3, and similarly in the mixing region the peak pair (2′, 3′) disappears at $X/D \simeq 1{\cdot}4$ as compared with $X/D \simeq 1{\cdot}2$ for the peak pair (6′, 7′). In the outer part of the mixing region ($\eta > 0$) most of the flow processes in the vortex pairing 2/3 were derived but the corresponding events identified for vortex 1 are more restricted. The outline of vortex 1 (e, f) can be identified back to $X/D \simeq 0{\cdot}8$, but close to the nozzle only the ejection path 5′ and the flow event e' could be recognized. The other flow events are of small scale or too remote in space and time to be derived by the time-domain technique using a fixed hot-wire probe at $X/D = 2{\cdot}0$.

It has thus been possible, using the new time-domain technique, to determine the separate flow events in the vortex structure 1 corresponding to the trigger event B, including the original formation of the vortex structure by a single vortex-pairing process. The two vortices which follow vortex 1 have been shown to be strongly related in space and time to the occurrence of flow event B, and their coalescence into a large vortex structure has also been clearly demonstrated.

Similar flow events occur continuously in the jet flow but, as we consider events further and further removed in time from the selected trigger event B, we find that they no longer occur regularly *relative to* the trigger event B. This accounts for the temporal and spatial limitations in the derivation of the large-scale flow structure.

9. General discussion

It has been demonstrated in the present paper for a moderate Reynolds number of 10^4 that the large-scale flow structure which is fixed relative to a selected trigger criterion can be derived from fixed hot-wire probes. The trigger criterion selected a particular large-scale flow event and the time-domain technique evaluated the other flow events which are fixed relative to the selected trigger event. The large-scale flow *structure* is very coherent at moderate Reynolds numbers, and the time-domain technique consequently determined all the regular large-scale flow events, the spatial

distribution (figures 14 and 16) of which constitutes the large-scale flow *structure* existing in the jet flow.

When the flow is more complex (e.g. turbulent jet flow) then the time-domain technique may evaluate either a separate large-scale flow event or a coherent flow structure. The trigger event selects a particular large-scale flow *event* but only if the surrounding fluid is coherent relative to the selected trigger event can the time-domain technique derive a regular large-scale flow *structure*. In part 2 of this study, for a turbulent air jet ($Re = 2 \times 10^5$), results for both separate large-scale flow events and more coherent flow structures will be presented.

The selected trigger event may be the occurrence of either a large positive or a large negative velocity peak, or it may be related to other flow parameters such as a shear-stress or a vorticity component. The time-domain technique was developed for the u velocity component, but in part 2 of this study it will be shown that the method can be extended to derive the related radial and circumferential velocity components. The data used in the time-domain analysis were obtained with hot-wire probes, but other velocity techniques such as hot-film or laser-Doppler anemometry are equally suitable, and the time-domain technique can be extended to other flow parameters such as density, pressure or temperature.

By using a hot-wire probe as a reference probe and a microphone as the moving probe one can determine the large-scale pressure field, which is fixed relative to the selected hot-wire trigger event. This type of information is of particular importance for jet-noise source location.

Any type of fluid flow can be investigated (e.g. jet flows, boundary-layer flows, flow around bluff bodies, etc.) and the type of trigger probe, trigger event and moving probe can be selected to evaluate a particular flow phenomenon. In each case the time-domain technique will yield the large-scale flow events which are fixed relative to the selected trigger event.

10. Conclusion

The large-scale flow structure existing in a transitional circular jet flow at a moderate Reynolds number of 10^4 has been derived by a new time-domain technique and the flow structure evaluated has been confirmed by a flow-visualization experiment. The temporal and spatial relationship of the separate flow events has also been determined and enabled the study of the flow development occurring in the large-scale structure:

(i) The spatial relationship between the induced potential-core fluctuations and the large-scale flow structure in the mixing region.

(ii) The flow paths for the ejection of the fast-moving potential-core fluid into the vortex structures.

(iii) The entrainment of fluid from the surrounding still air behind the vortex structures.

(iv) The spatial growth of the vortex structure 1 corresponding to the selected trigger event.

(v) The timewise variation of the spatial separation between vortex structures 1, 2 and 3.

(vi) The coalescence of vortex structures 2 and 3, which follow vortex structure 1.

The corresponding results for a high Reynolds number turbulent jet are presented in part 2 of this study.

The experimental part of this study was carried out while the author was a research fellow at the Institute of Sound and Vibration Research, Southampton University. The work was part of a major SRC grant awarded to Professor P. O. A. L. Davies to study turbulent flow structures using time-domain analysis. The other members of the team were Dr A. J. Yule and Mr D. R. J. Baxter. Further data and experimental details are available in the first three annual progress reports (*ISVR Int. Publ.* memos. 489, 506 and 529). The author also wishes to thank Dr M. J. Fisher for his advice.

REFERENCES

BECKER, H. A. & MASSARO, T. A. 1968 Vortex evolution in a round jet. *J. Fluid Mech.* **31**, 435–448.

BRADSHAW, P., FERRISS, D. H. & JOHNSON, R. F. 1964 Turbulence in the noise-producing region of a circular jet. *J. Fluid Mech.* **19**, 591–624.

BRUUN, H. H. 1971 Linearization and hot-wire anemometry. *J. Sci. Instr.* **4**, 815–820.

BRUUN, H. H. 1975 On the temperature dependence of constant temperature hot-wire probes with small wire aspect ratio. *J. Sci. Instr.* **8**, 942–951.

BRUUN, H. H. 1976 A digital comparison of linear and non-linear hot-wire data evaluation. *J. Sci. Instr.* **9**, 53–57.

CROW, S. C. & CHAMPAGNE, F. H. 1971 Orderly structure in jet turbulence. *J. Fluid Mech.* **48**, 547–591.

DAVIES, P. O. A. L. 1974 The ISVR constant temperature hot-wire anemometer. *Southampton Univ. ISVR Rep.* no. 66.

DAVIES, P. O. A. L., FISHER, M. J. & BARRATT, M. J. 1963 The characteristics of turbulence in the mixing region of a round jet. *J. Fluid Mech.* **15**, 337–367.

FREYMUTH, P. 1966 On transition in a separated laminar boundary layer. *J. Fluid Mech.* **25**, 683–704.

KO, N. W. M. & DAVIES, P. O. A. L. 1971 The near field within the potential cone of subsonic cold jets. *J. Fluid Mech.* **50**, 49–78.

KO, N. W. M. & DAVIES, P. O. A. L. 1975 Some covariance measurements in a subsonic jet. *J. Sound Vib.* **41**, 347–358.

LAU, J. C. & FISHER, M. J. 1975 The vortex-street structure of 'turbulent' jets. Part 1. *J. Fluid Mech.* **67**, 299–337.

LAU, J. C., FISHER, M. J. & FUCHS, H. V. 1972 The intrinsic structure of turbulent jets. *J. Sound Vib.* **22**, 379–406.

WEHRMANN, O. & WILLE, R. 1958 Beitrag zur Phänomenologie des laminar-turbulenten Übergangs im Freistrahl bei kleinen Reynolds-Zahlen. *Boundary-Layer Res.* In *Boundary-Layer Research* (ed. H. Görtler), pp. 387–403. Springer.

WILLE, R. 1963 Beiträge zur Phänomenologie der Freistrahlen. *Z. Flugwiss.* **6**, 222–232.

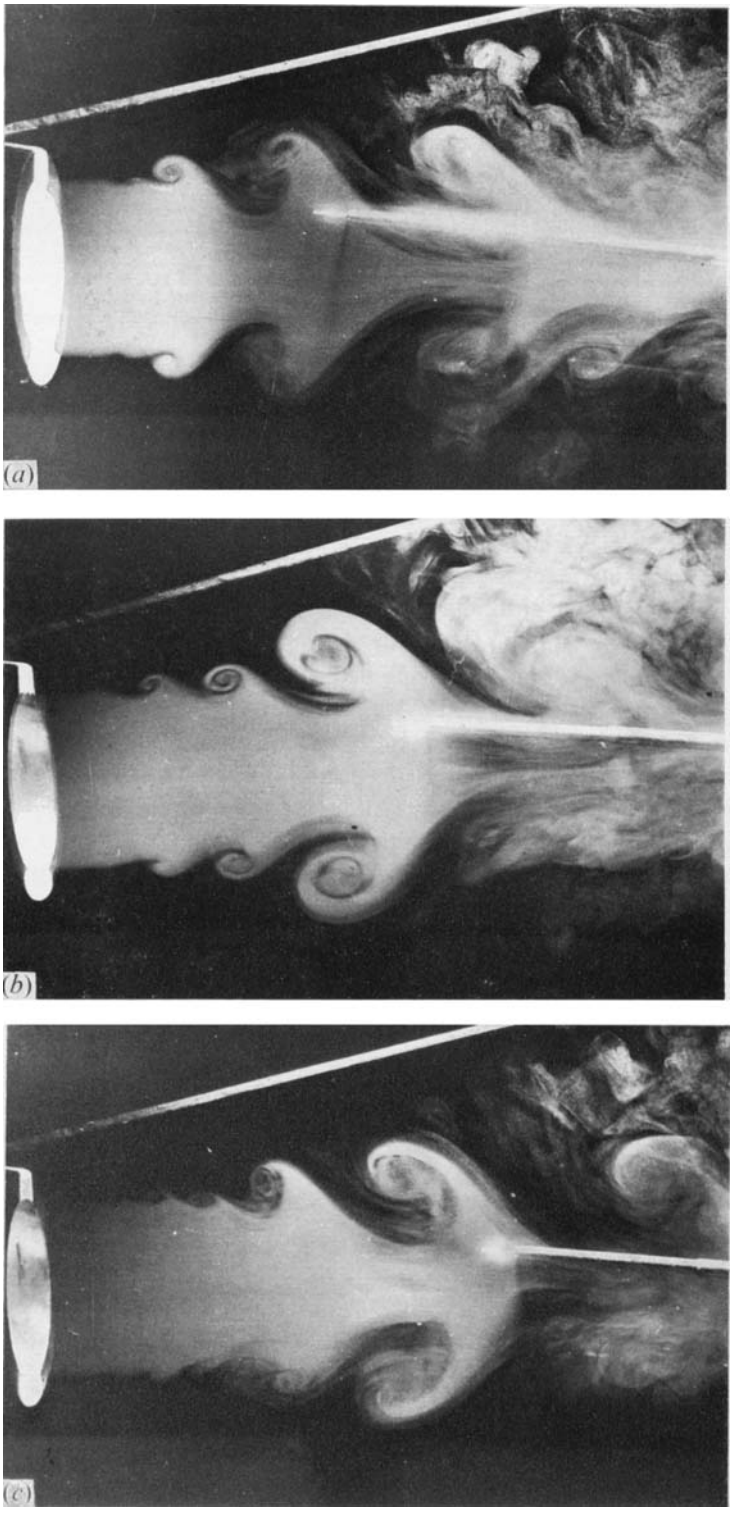

FIGURE 6. Smoke flow-visualization photographs corresponding to a large positive peak occurring at (*a*) $X/D = 1{\cdot}5$, (*b*) $X/D = 2{\cdot}0$ and (*c*) $X/D = 2{\cdot}5$ for $\eta = -0{\cdot}15$. Notice the final stage of a vortex pairing at $X/D \simeq 1{\cdot}5$ in (*a*).